

A Multifidelity Approach to Robust Orbit Determination

Alberto Fossà^{1,*}, Roberto Armellin², Emmanuel Delande³, Matteo Losacco¹, and
Francesco Sanfedino¹

¹*Department of Aerospace Vehicles Design and Control, Institut Supérieur de
l'Aéronautique et de l'Espace, 10 Avenue Edouard Belin, Toulouse, 31055, France*

²*Te Pūnaha Ātea - Space Institute, The University of Auckland, 20 Symonds Street,
Auckland, 1010, New Zealand*

³*Space Situational Awareness Office, Centre National d'Études Spatiales, 18 Avenue
Edouard Belin, Toulouse, 31400, France*

* *Corresponding author, alberto.fossa@isae-superaero.fr*

Abstract

This paper presents an algorithm for the preprocessing of observation data aimed at improving the robustness of orbit determination tools. Two objectives are fulfilled: obtain a refined solution to the initial orbit determination problem and detect possible outliers in the processed measurements. The uncertainty on the initial estimate is propagated forward in time and progressively reduced by exploiting sensor data available in said propagation window. Differential algebra techniques and a novel automatic domain splitting algorithm for second-order Taylor expansions are used to efficiently propagate uncertainties over time. A multifidelity approach is employed to minimize the computational effort while retaining the accuracy of the propagated estimate. At each observation epoch, a polynomial map is obtained by projecting the propagated states onto the observable space. Domains that do not overlap with the actual measurement are pruned thus reducing the uncertainty to be further propagated. Measurement outliers are also detected in this step. The refined estimate and pruned observations are then used to improve the robustness of batch orbit determination tools. The effectiveness of the algorithm is demonstrated for a geostationary transfer orbit object using synthetic and real observation data from the TAROT network.

Keywords: uncertainty propagation, multifidelity methods, robust orbit determination

1 Introduction

Preserving the realism of the probabilistic representation of space objects (SOs) states over time is paramount in space situational awareness (SSA) applications

such as orbit determination (OD) and SOs catalogs build-up and maintenance. To accomplish these tasks, two main tools are required: an accurate and efficient uncertainty propagation (UP) method and an effective strategy to incorporate newly available information in the predicted estimate. This work contributes to these needs by proposing a pruning algorithm for the refinement of an initial solution, typically the result of an initial orbit determination (IOD) process, and the detection of measurements outliers among the input set. The algorithm is composed of four main steps which are carried out sequentially for each available measurements: propagation of the current state estimate, projection onto the observable space, pruning of the uncertainty based on the newly available information, and merging to reduce the information to be further propagated.

Regarding the UP problem in orbital dynamics, this has been historically tackled with either linearized methods or large scale Monte Carlo (MC) simulations. Several methods for nonlinear UP have since been proposed and are conveniently classified as intrusive or non-intrusive, with the first requiring full knowledge of the underlying dynamics while the seconds treating the dynamical model as a *black box*. The first category includes State Transition Tensors (STTs) [1] and differential algebra (DA) [2, 3] while the second gathers the aforementioned MC as well as unscented transform (UT) [4], conjugate unscented transform (CUT) [5] and polynomial chaos expansions (PCEs) [6]. A comprehensive survey of these methods can be found in [7]. In this work, DA is used for UP in conjunction with an automatic domain splitting (ADS) algorithm [8] to control the error on the final solution manifold. Multifidelity methods are exploited to drastically reduce the computational effort of the overall algorithm while retaining a similar accuracy on the final solution. Their effectiveness for orbit UP was already demonstrated in [9, 10] and corroborated in this work. The DA-based UP is carried out on a low-fidelity dynamical model and only the centers of the resulting manifold are propagated in high-fidelity to compute a posteriori correction to the low-fidelity solution.

The projection onto the observables space follows, also wrapped by the ADS algorithm to retain the accuracy of the resulting polynomial map, or manifold, that represents the uncertainty on the predicted measurements by patching a set of truncated Taylor expansions. Polynomial bounding techniques are then employed to estimate the range of variation of both predicted and actual measurements. These bounds are then used to discard the domains that do not match the real observation and reduce the size of the manifold of states to be further propagated. Possible measurements outliers are also identified in the observations that have no intersection with the projected set. The output is a refined solution to the IOD problem that is used as improved guess to initialize a batch OD algorithm. Concerning the last, if least squares (LS) techniques are the workhorse of current

operational algorithms, a more robust approach to the OD problem, named least sum of absolute residuals (LSAR), was recently proposed in [11]. Both solutions are compared in this paper highlighting the benefits provided by the pruning algorithm over a direct processing of all available information. A complete solution to the batch OD problem is thus presented, with DA being the common denominator underlying each proposed tool. This approach is demonstrated of being robust to measurements outliers thanks to an effective preprocessing of the available observations and the use of the LSAR algorithm to compute the final estimate.

The paper is organized as follows. DA-based UP and automatic domain splitting are firstly introduced in Section 2. The IOD algorithm is presented in Section 3.2 followed by a description of the MF technique in Sections 3.3 and 3.4. The pruning scheme is presented in Sections 3.5 to 3.7 before the batch OD algorithms which are described in Section 3.8. Numerical applications of the proposed tool are presented in Section 4 before drawing the conclusions in Section 5.

2 Mathematical background

This section describes the main tools on which this work is built on. These include differential algebra techniques applied to uncertainty propagation and the automatic domain splitting and merging algorithms used to control the accuracy of Taylor expansions.

2.1 Differential algebra

Differential algebra is a computing technique based on the idea that it is possible to extract more information from a function f than its mere value $y = f(x)$ at x . It replaces the algebra of floating point (FP) numbers with a new algebra of Taylor polynomials to compute the given order Taylor expansion of any function f in v variables that is \mathcal{C}^{n+1} in the domain of interest $[-1, 1]^v$ [2]. The notation used is

$$f \approx [f] = \mathcal{T}_f(\delta\mathbf{x}) \quad (1)$$

where $\delta\mathbf{x} = \{\delta x_1, \dots, \delta x_v\}^T$ are the v independent DA variables.

As for the FP algebra, the four arithmetic operations ($+$, $-$, $*$, \div), implicit functions (e.g. trigonometric functions, powers, exponential and logarithm), derivation, integration, function composition and inversion are well defined in DA. The latter technique is particularly suitable for the solution of implicit equations and the computation of the Taylor expansion of the flow of differential equations in terms of their initial conditions.

2.2 Polynomial bounding

Consider the DA of order n in v variables, and a multivariate polynomial $p(\delta\mathbf{x})$ with coefficients $a_k \in \mathbb{R}$. Define as *odd* the coefficients for which at least one DA variable appears with an odd exponent (e.g. δx_1 or $\delta x_1^2 \delta x_2$), and denote them with the superscript “ o ”. Likewise, define as *even* coefficients those for which all variables appear with even exponents (e.g. δx_1^2 or $\delta x_1^2 \delta x_2^2$), and denote them with the superscript “ e ”. Since $\delta\mathbf{x} \in [-1, 1]^v$, an estimation of the range of variation, or bounds, of $p(\delta\mathbf{x})$ can be obtained as

$$\begin{aligned} b_l &= a_0 - \sum_{k=1}^{n_o} |a_k^o| + \sum_{k=1}^{n_e} \min\{0, a_k^e\} \\ b_u &= a_0 + \sum_{k=1}^{n_o} |a_k^o| + \sum_{k=1}^{n_e} \max\{0, a_k^e\} \end{aligned} \quad (2)$$

with b_l, b_u lower and upper bounds such that $p(\delta\mathbf{x}) \in [b_l, b_u]$, a_0 constant part and n_o, n_e number of odd and even coefficients respectively. For first-order polynomials the bounds computed with Eq. (2) are rigorous in the sense that they coincide with the extrema of $p(\delta\mathbf{x})$ when evaluated in $[-1, 1]^v$. In this case all even coefficients are identically zero and Eq. (2) simplifies to

$$p(\delta\mathbf{x}) \in \left[a_0 \pm \sum_{k=1}^v |a_k^o| \right] \quad (3)$$

2.3 Uncertainty propagation

Given the nonlinear transformation $\mathbf{f} : \mathbb{R}^n \rightarrow \mathbb{R}^m$ and two multivariate random variables \mathbf{X}, \mathbf{Y} with probability density function (pdf) $p_{\mathbf{X}}, p_{\mathbf{Y}}$ respectively, the UP problem requires the estimation of $p_{\mathbf{Y}}$ from the only knowledge of $p_{\mathbf{X}}$ and \mathbf{f} . In DA framework, \mathbf{X} is represented as a vector of first-order multivariate polynomials in the form

$$[\mathbf{x}] = \bar{\mathbf{x}} + \boldsymbol{\beta} \odot \delta\mathbf{x} \quad (4)$$

with $\bar{\mathbf{x}} = \mathbb{E}[\mathbf{X}]$ the expected value of \mathbf{X} , $\boldsymbol{\beta}$ the semi-amplitude of the range of variation of $[\mathbf{x}]$, $\delta\mathbf{x}$ the first-order variations of \mathbf{X} around $\bar{\mathbf{x}}$ and \odot the Hadamard (or element-wise) product. The Taylor expansion of \mathbf{Y} in terms of $\delta\mathbf{x}$ is then obtained evaluating \mathbf{f} in DA framework as

$$[\mathbf{y}] = \mathbf{f}([\mathbf{x}]) = \mathcal{T}_{\mathbf{y}}(\delta\mathbf{x}) \quad (5)$$

In the context of UP, different methods were proposed to efficiently compute the statistical properties of \mathbf{Y} from $\mathcal{T}_{\mathbf{y}}(\delta\mathbf{x})$ thus avoiding the needs for expensive Monte Carlo (MC) simulations [3].

2.4 Low-order automatic domain splitting

Taylor polynomials are only a local approximation of the function \mathbf{f} around the expansion point, and a single polynomial might fail to accurately represent the uncertainty for $|\delta\mathbf{x}| \gg 0$. To overcome this limitation, automatic domain splitting (ADS) was firstly proposed by [8] to monitor the accuracy of the expansion at the edges of its domain and recursively split the initial polynomial into smaller subdomains in which the required accuracy is satisfied.

Instead, a novel splitting technique specific for second-order Taylor polynomials is used in this work [10, 12]. The algorithm, named low-order automatic domain splitting (LOADS), defines a nonlinearity index (NLI) computed from the Jacobian of the transformation $\partial\mathbf{f}/\partial\mathbf{x}$ that was inspired by the nonlinearity measure introduced by [13]. In this paper, \mathbf{f} is referred as the *target* function of the LOADS scheme.

Given an initial domain $[\mathbf{x}^{(0)}]$, the algorithm starts by evaluating \mathbf{f} in $[\mathbf{x}^{(0)}]$ and computing the NLI of the output $[\mathbf{y}^{(0)}]$ as follows.

The Jacobian of the transformation is firstly computed as the sum of its constant part $\bar{\mathbf{J}}$ and first-order expansion $\delta\mathbf{J}(\delta\mathbf{x})$ as

$$[\mathbf{J}] = \frac{\partial\mathbf{f}}{\partial\mathbf{x}} = \bar{\mathbf{J}} + \delta\mathbf{J} \quad (6)$$

since $\delta\mathbf{J} \equiv \mathbf{0}$ for a linear transformation, a measure of nonlinearity can be obtained from the magnitude of $\delta\mathbf{J}$. For each entry δJ_{ij} , rigorous bounds are firstly obtained from Eq. (2) as

$$b_{ij} = \sum_{k=1}^n |a_{ij,k}| \quad (7)$$

where $a_{ij,k}$ are the first-order coefficients of J_{ij} , i.e. $\delta J_{ij} = \sum_{k=1}^n a_{ij,k} \delta x_k$ and thus $\delta J_{ij} \in [-b_{ij}, b_{ij}]$. The nonlinearity index is then defined as

$$\nu = \frac{\sqrt{\sum_{i=1}^m \sum_{j=1}^n (\sum_{k=1}^n |a_{ij,k}|)^2}}{\sqrt{\sum_{i=1}^m \sum_{j=1}^n \bar{J}_{ij}^2}} \quad (8)$$

which is the ratio between the Frobenius norm of the matrix of the bounds and the Frobenius norm of the constant part of the Jacobian $\bar{\mathbf{J}}$.

The computed NLI is then compared with an imposed error threshold ε and a decision is made. If $\nu \leq \varepsilon$ the algorithm ends and $[\mathbf{y}^{(0)}]$ is retained. On the contrary, if $\nu > \varepsilon$, the output is rejected and $[\mathbf{x}^{(0)}]$ is split into three polynomials $[\mathbf{x}^{(j)}]$ with each one covering 1/3 of the initial domain.

To perform the split, a second index is firstly computed to identify the direction that contributes the most to the nonlinearity in $[\mathbf{y}]$. For each independent DA

variable δx_d , a directional Jacobian is built as the function composition of $[\mathbf{J}]$ and $\delta \mathbf{x}_d$ as

$$[\mathbf{J}_d] = [\mathbf{J}] \circ \delta \mathbf{x}_d \quad (9)$$

where $\delta \mathbf{x}_d$ is a vector of zeros except for the d^{th} component set equal to δx_d , i.e. $\delta \mathbf{x}_d = \{0, \dots, \delta x_d, \dots, 0\}^T$, and \circ denotes function composition. A directional NLI ν_d is then computed from $[\mathbf{J}_d]$ as in Eq. (8) and the splitting direction d_s selected for the maximum ν_d

$$d_s = \arg \max_d \{\nu_d\} \quad (10)$$

Knowing d_s , the three subdomains $[\mathbf{x}^{(j)}]$ for $j \in [1, 3]$ are computed from $[\mathbf{x}^{(0)}]$ as

$$[\mathbf{x}^{(j)}] = [\mathbf{x}^{(0)}] \circ \left\{ 0, \dots, \frac{2}{3} \cdot (j-2) + \frac{1}{3} \cdot \delta x_{d_s}, \dots, 0 \right\}^T \quad (11)$$

The target function is then evaluated on the set $\{[\mathbf{x}^{(j)}]\}$ and the procedure iterated until the accuracy is satisfied in each subdomain. The result is a set of polynomials for both the initial domain and its image through \mathbf{f} . These sets are named *manifolds* and denoted as $M_{\mathbf{x}} = \{[\mathbf{x}^{(i)}]\}$ and $M_{\mathbf{y}} = \{[\mathbf{y}^{(i)}]\}$ respectively where $i \in [1, N]$ and N is the total number of domains after splitting.

2.5 Domain merging

Consider a second function $\mathbf{g} : \mathbb{R}^m \rightarrow \mathbb{R}^p$ evaluated on the manifold $M_{\mathbf{y}}$ to obtain $M_{\mathbf{z}}$. Nonlinearities in $[\mathbf{z}^{(i)}]$ can be smaller than that of $[\mathbf{y}^{(i)}]$ and one or more NLIs computed from $\partial \mathbf{g} / \partial \mathbf{y}$ can fall far below the splitting threshold, i.e. $\nu^{(i)} \ll \varepsilon$. In this case it is thus conceivable to develop an algorithm to recombine the polynomials $[\mathbf{z}^{(i)}]$ and reduce the size of $M_{\mathbf{z}}$. The merging scheme used in this work stems from this observation and requires the knowledge of the entire *splitting history* of each polynomial in $M_{\mathbf{z}}$ to attempt a recombination of the different domains [12]. This information comprises all directions d_s and shifts j along which $[\mathbf{z}^{(i)}]$ was split and allows to identify domains that generated from the same parent and thus potentially mergeable.

Given the manifold $M_{\mathbf{z}}$, the merging scheme proceeds as follows. Firstly, the domains are grouped by *depth* of split, i.e. by the number of times they have been split. Secondly, starting from the sub-manifold with the greatest depth, the histories of its elements are compared to identify all triplets sharing a common parent. For each triplet, the domain of the parent is recovered as

$$[\mathbf{z}^{(i)}] = [\mathbf{z}^{(2)}] \circ \{0, \dots, 3\delta x_{d_s}, \dots, 0\}^T \quad (12)$$

with d_s last splitting direction and $[\mathbf{z}^{(2)}]$ central polynomial. A decision on the potential merge is then taken after computing the NLI of $[\mathbf{z}^{(i)}]$: if $\nu \leq \varepsilon$, $[\mathbf{z}^{(i)}]$ is

retained and added to the sub-manifold with a shallower depth. if $\nu > \varepsilon$, $[\mathbf{z}^{(i)}]$ is discarded and the three domains of the original triplet added to the final manifold M'_z . This procedure is repeated until all sub-manifolds have been emptied. At each stage, if an incomplete triplet is found, no merge is attempted and its elements are directly added to M'_z .

3 Robust orbit determination

The full batch orbit determination chain is presented in this section. Given the space object (SO) of interest, an estimate of its orbit state at epoch t_0 is firstly obtained with the DA-based initial orbit determination (IOD) routine described in Section 3.2. This estimate is then propagated forward in time using multifidelity techniques to minimize the computational effort and its uncertainty progressively reduced with a custom pruning scheme as soon as new measurements become available. Potential outliers in the input measurements are also identified and discarded in this step. A batch OD algorithm is finally run on the pruned state and retained observations to compute the final estimate. Both LS and LSAR techniques are tested and their performance discussed in Section 4. The overall workflow is summarized in Fig. 1. This paper assumes observations from optical telescopes, but the tools can be easily extended to other types of measurements.

3.1 Measurement model

Consider an optical telescope identified by its geodetic coordinates (ϕ, λ, h) with $\phi \in [-\pi/2, \pi/2]$ geodetic latitude, $\lambda \in [-\pi, \pi]$ geodetic longitude and $h \in \mathbb{R}^+$ geodetic height. Denote with $\mathbf{x} = [\mathbf{r} \ \mathbf{v}]^T$ the inertial state vector of the tracked SO and with \mathbf{r}_{obs} the inertial position of the telescope at the same epoch. The two positions $\mathbf{r}, \mathbf{r}_{obs}$ are related by

$$\mathbf{r} = \mathbf{r}_{obs} + \rho \hat{\boldsymbol{\rho}} \quad (13)$$

with ρ topocentric range and $\hat{\boldsymbol{\rho}}$ line of sight (LOS) unit vector. The last is computed from the topocentric right ascension and declination (α, δ) as

$$\hat{\boldsymbol{\rho}} = \begin{bmatrix} \cos \alpha \cos \delta \\ \sin \alpha \cos \delta \\ \sin \delta \end{bmatrix} \quad (14)$$

If the LOS vector $\rho\hat{\boldsymbol{p}} = [\rho_x \ \rho_y \ \rho_z]^T$ is known instead, the topocentric range, right ascension and declination are given by

$$\begin{cases} \rho = \sqrt{\rho_x^2 + \rho_y^2 + \rho_z^2} \\ \alpha = \tan^{-1} \rho_y / \rho_x \\ \delta = \sin^{-1} \rho_z / \rho \end{cases} \quad (15)$$

3.2 Initial orbit determination

Consider a set of N tuples of angular measurements as provided by a ground based optical sensor while observing an unknown SO

$$\{t_i; (\alpha_i; \sigma_{\alpha_i}), (\delta_i; \sigma_{\delta_i})\} \quad i \in [1, N] \quad (16)$$

with α_i, δ_i topocentric right ascension and declination of the SO at epoch t_i and $\sigma_{\alpha_i}, \sigma_{\delta_i}$ associated standard deviations of the sensor noise, assumed as uncorrelated white noise.

The goal of the IOD is to estimate the state of the object from the available set of measurements. The problem is well-known in literature and typically solved by processing the nominal angular measurements only [14, 15]. The approach here exploited was firstly developed by [16] and makes use of DA to obtain an analytic map between the confidence intervals of the processed measurements and the uncertainty of the computed solution. The method sets up an iterative procedure to estimate the topocentric ranges of the object at the epoch of the first, middle, and last available measurements, namely $\rho_k = \{\rho_1, \rho_2, \rho_3\}$. The initial guess for these ranges is provided by the classical Gauss solution [15]. Two Lambert's problems [17] are then solved between t_1, t_2 and t_2, t_3 respectively. A nonlinear solver is then used to update ρ_j such that the velocity vectors at the intermediate epoch coincide. An estimate of the object state is then directly available from this solution.

A polynomial expansion of the state with respect to the observables can be obtained by initializing the processed measurements as Taylor variables and performing all operations in the DA framework. In this case

$$\begin{aligned} [\boldsymbol{\alpha}] &= \boldsymbol{\alpha} + c\boldsymbol{\sigma}_{\boldsymbol{\alpha}} \odot \delta\boldsymbol{\alpha} \\ [\boldsymbol{\delta}] &= \boldsymbol{\delta} + c\boldsymbol{\sigma}_{\boldsymbol{\delta}} \odot \delta\boldsymbol{\delta} \end{aligned} \quad (17)$$

with c the confidence interval and

$$\begin{aligned} \boldsymbol{\alpha} &= [\alpha_1 \ \alpha_2 \ \alpha_3]^T & \boldsymbol{\sigma}_{\boldsymbol{\alpha}} &= [\sigma_{\alpha_1} \ \sigma_{\alpha_2} \ \sigma_{\alpha_3}]^T \\ \boldsymbol{\delta} &= [\delta_1 \ \delta_2 \ \delta_3]^T & \boldsymbol{\sigma}_{\boldsymbol{\delta}} &= [\sigma_{\delta_1} \ \sigma_{\delta_2} \ \sigma_{\delta_3}]^T \end{aligned} \quad (18)$$

The state vectors at t_j can then be written as

$$[\mathbf{x}_j] = \mathcal{T}_{\mathbf{x}_j}(\delta\boldsymbol{\alpha}, \delta\boldsymbol{\delta}) \quad j \in [1, 3] \quad (19)$$

The solution in Eq. (19) is obtained under the assumption of unperturbed Keplerian motion (since based on the recursive solution of two Lambert problems) and might be inaccurate for long observation windows in which deviations from the nominal two-body trajectory cannot be neglected. A DA-based shooting scheme is thus employed to account for the effects of the J_2 term of the Earth's gravitational potential. Given the needs for a fast propagation method at this stage, the analytical formulation of the J_2 -perturbed dynamics proposed in [18] is employed. Starting from Eq. (19), an updated estimate is then obtained as

$$[\mathbf{x}_j^{J_2}] = \mathcal{T}_{\mathbf{x}_j^{J_2}}(\delta\boldsymbol{\alpha}, \delta\boldsymbol{\delta}) \quad j \in [1, 3] \quad (20)$$

3.3 State Noise Compensation

Taking into account the uncertainty due to neglected or mismodeled accelerations is paramount to achieve a precise estimate of the propagated orbit. Stochastic accelerations are thus included in the developed UP framework and their effects on the state covariance estimated using the State Noise Compensation (SNC) algorithm [19].

For continuous systems, the dynamics under the influence of process noise is described by

$$\dot{\mathbf{x}} = \mathbf{f}(\mathbf{x}, t) + \mathbf{B}(t)\mathbf{w}(t) \quad (21)$$

with $\mathbf{f} : \mathbb{R}^n \times \mathbb{R} \rightarrow \mathbb{R}^n$ the deterministic dynamics, $\mathbf{w}(t)$ the m -dimensional process noise, and $\mathbf{B}(t)$ the $n \times m$ *process noise mapping matrix* that maps the process noise into state derivatives. Under the assumption of uncorrelated white noise, the first two statistical moments of $\mathbf{w}(t)$ are given by

$$\begin{aligned} \mathbb{E}[\mathbf{w}(t)] &= \mathbf{0} \\ \mathbb{E}[\mathbf{w}(t)\mathbf{w}^T(t)] &= \mathbf{Q}(t)\delta(t - \tau) \end{aligned} \quad (22)$$

with $\delta(t - \tau)$ the Dirac delta and $\mathbf{Q}(t)$ the process noise covariance matrix. An estimate of the true state is then maintained through a mean state $\mathbf{x}(t)$ and a covariance matrix $\mathbf{P}(t)$ that are computed by integrating the system of first-order ordinary differential equations (ODEs)

$$\begin{cases} \dot{\mathbf{x}}(t) &= \mathbf{f}(\mathbf{x}, t) \\ \dot{\mathbf{P}}(t) &= \mathbf{A}(t)\mathbf{P}(t) + \mathbf{P}(t)\mathbf{A}^T(t) + \mathbf{B}(t)\mathbf{Q}(t)\mathbf{B}^T(t) \end{cases} \quad (23)$$

subject to initial conditions $\mathbf{x}(t_0) = \mathbf{x}_0$ and $\mathbf{P}(t_0) = \mathbf{0}$.

3.4 Multifidelity uncertainty propagation

Multifidelity methods are introduced to improve the computational efficiency of the prediction step while guaranteeing the required accuracy for the final estimate. In particular, a bifidelity technique based on two distinct dynamical models is employed.

The low-fidelity model is the Simplified General Perturbations (SGP4) model used by NORAD to produce daily Two-Line Elements (TLEs) of all tracked SOs [20]. Given its analytical formulation, SGP4 is easily embedded in the DA-LOADS framework to efficiently propagate orbit states and associated uncertainties as Taylor polynomials. An high-fidelity correction is yet needed to retain the accuracy of the final solution. A numerical propagator is thus used to integrate the high-fidelity orbital dynamics as well as the effects of process noise via Eq. (23). In this work, $\mathbf{f}(\mathbf{x}, t)$ are the Gauss variational equations which describe the motion of SOs in the perturbed Keplerian dynamics [21].

Given some prior information on the object's state at t_0 , represented as a manifold of Taylor polynomials $M(t_0) = \{[\mathbf{x}^{(i)}(t_0)]\}$, the solution manifold $M(t_1)$ at target time t_1 is computed as follows. Firstly, $M(t_0)$ is processed with the LOADS scheme setting SGP4 as target function \mathbf{f} . The results is a low-fidelity solution manifold $M_{LF}(t_1)$ whose size is generally different from that of $M(t_0)$. In the second step, the centers of the polynomials $[\mathbf{x}^{(i)}(t_0)]$ that maps to $[\mathbf{x}^{(i)}(t_1)]$ in $M_{LF}(t_1)$ are propagated point-wise in high-fidelity using Eq. (23) to obtain the reference solutions $\{\mathbf{x}_{HF}^{(i)}(t_1)\}$ and covariance matrices $\{\mathbf{P}_{PN}^{(i)}(t_1)\}$ for each polynomial in $M_{LF}(t_1)$. Note that these covariances are the result of the effects of process noise and do not include the contribution of the initial uncertainty which was already taken into account in the low-fidelity step. The multifidelity solution is then computed re-centering the Taylor expansions in $M_{LF}(t_1)$ on the high-fidelity trajectories $\{\mathbf{x}_{HF}^{(i)}(t_1)\}$ and inflating the uncertainties due to ICs with the contribution of process noise. Each covariance matrix $\mathbf{P}_{PN}^{(i)}(t_1)$ is represented in the DA framework as

$$[\mathbf{x}_{PN}^{(i)}(t_1)] = \mathbf{V}^{(i)} \cdot \left(c\sqrt{\boldsymbol{\lambda}^{(i)}}\delta\mathbf{x} \right) \quad (24)$$

with c the confidence interval, $\mathbf{P}_{PN}^{(i)}(t_1) = \mathbf{V}^{(i)}\boldsymbol{\Lambda}^{(i)}\left(\mathbf{V}^{(i)}\right)^T$ the covariance matrix eigendecomposition, and $\boldsymbol{\lambda}^{(i)}$ the main diagonal of $\boldsymbol{\Lambda}^{(i)}$. Then, the i^{th} domain of the manifold at target time t_1 is given by the multifidelity expansion

$$[\mathbf{x}_{MF}^{(i)}(t_1)] = \mathbf{x}_{HF}^{(i)}(t_1) + \left\{ [\mathbf{x}_{LF}^{(i)}(t_1)] - \bar{\mathbf{x}}_{LF}^{(i)}(t_1) \right\} + [\mathbf{x}_{PN}^{(i)}(t_1)] \quad (25)$$

which is a Taylor polynomial centered at $\mathbf{x}_{HF}^{(i)}(t_1)$ and whose non-constant coefficients model the uncertainty due to both ICs and stochastic accelerations.

For computational purposes, alternate equinoctial elements are used for propagation. This set of coordinates is defined in terms of the six Keplerian parameters as [22]

$$\begin{aligned}
n &= \sqrt{\mu/a^3} \\
f &= e \cos(\omega + \Omega) \\
g &= e \sin(\omega + \Omega) \\
h &= \tan(i/2) \cos(\Omega) \\
k &= \tan(i/2) \sin(\Omega) \\
\lambda &= \Omega + \omega + M
\end{aligned} \tag{26}$$

with a the semi-major axis, e the eccentricity, i the inclination, Ω the right ascension of the ascending node, ω the argument of periapsis, and M the mean anomaly, where n is the mean motion, and λ the mean longitude. Given the quasi-linearity of the ODEs governing their evolution over time in perturbed Keplerian dynamics, this choice leads to smaller number of domains generated in the low-fidelity step compared to either Cartesian, Keplerian or (modified) equinoctial parameters [23, 24].

3.5 Projection onto observables space

Consider a set of osculating orbital elements $\mathbf{x}(t_k)$ at epoch t_k and an optical telescope as described in Section 3.1. The spherical coordinates $(\rho_k, \alpha_k, \delta_k)$ of the SO as seen from the telescope at epoch t_k are given by Eq. (15) with $\boldsymbol{\rho} = [\rho_x \ \rho_y \ \rho_z]^T$ LOS vector obtained from Eq. (13). Moreover, the SO's position \mathbf{r}_k is easily obtained by transforming $\mathbf{x}(t_k)$ to Cartesian parameters.

In this work, all operations are carried out in the DA framework using the LOADS algorithm to project a manifold of orbit states $M_{\mathbf{x}}(t_k)$ onto a manifold of observables $M_{\hat{\mathbf{y}}}(t_k)$ with $\hat{\mathbf{y}}_k = [\hat{\alpha}_k \ \hat{\delta}_k]^T$ before the pruning step.

3.6 Domain pruning

Consider the manifold of observables $M_{\hat{\mathbf{y}}}(t_k)$ estimated from $M_{\mathbf{x}}(t_k)$ as in Section 3.5 and the real measurements (α_k, δ_k) taken from the same telescope at epoch t_k . The pruning algorithm seeks to reduce the size of $M_{\hat{\mathbf{y}}}(t_k)$, and thus $M_{\mathbf{x}}(t_k)$, exploiting the new information obtained from the sensor. The real measurements are firstly initialized as a DA vector

$$[\mathbf{y}] = \begin{bmatrix} \alpha_k \\ \delta_k \end{bmatrix} + c \cdot \begin{bmatrix} \sigma_{\alpha_k} \\ \sigma_{\delta_k} \end{bmatrix} \odot \delta \mathbf{y} \tag{27}$$

with c the confidence interval, $\sigma_{\alpha_k}, \sigma_{\delta_k}$ the 1σ uncertainty on α_k, δ_k , respectively, and $\delta \mathbf{y}$ the first-order deviations in α_k, δ_k . Rigorous bounds on $[\mathbf{y}]$ are then given

by the square interval $[\alpha_k \pm c \cdot \sigma_{\alpha_k}] \times [\delta_k \pm c \cdot \sigma_{\delta_k}]$ which is a simplification of Eq. (2) for first-order univariate polynomials.

For each domain in $M_{\hat{\mathbf{y}}}(t_k)$, its bounds are then estimated via Eq. (2) and compared with the ones above. If the two intervals overlap, the domain is retained for the subsequent steps. The polynomial is otherwise discarded from both $M_{\hat{\mathbf{y}}}(t_k)$ and $M_{\mathbf{x}}(t_k)$ since it is unlikely to include the true, yet unknown, orbit state. Similarly, if no intersection is found between $M_{\hat{\mathbf{y}}}(t_k)$ and $[\mathbf{y}]$, the measurement is deemed to be an outlier and no pruning is performed. The observation is subsequently excluded from the set processed with the batch OD algorithm described in Section 3.8.

3.7 Sequential prediction and pruning

The overall algorithm for the prediction and pruning of orbit states is presented in this section. Starting from the ICs $[\mathbf{x}(t_0)] = \mathcal{T}_{\mathbf{x}(t_0)}(\delta\boldsymbol{\alpha}, \delta\boldsymbol{\delta})$ obtained in Section 3.2, a sequential procedure is implemented to progressively tighten the bounds on $(\delta\boldsymbol{\alpha}, \delta\boldsymbol{\delta})$ by exploiting the information available from subsequent measurements.

The estimated Cartesian state is firstly transformed into alternate equinoctial elements. This transformation is evaluated in the DA framework using the LOADS scheme and the transformed ICs are thus represented as a manifold of polynomials $M_{\mathbf{x}}(t_0)$ function of $(\delta\boldsymbol{\alpha}, \delta\boldsymbol{\delta})$.

The measurement collected at time t_k is denoted by (α_k, δ_k) , $1 \leq k \leq M$, and the associated 1σ uncertainties by $(\sigma_{\alpha_k}, \sigma_{\delta_k})$, such that the developed algorithm requires M sequential steps to estimate $M_{\mathbf{x}}(t_M)$ from $M_{\mathbf{x}}(t_0)$ while exploiting the information available from the measurements. Each step k is further subdivided into the following operations

1. Propagation of $M_{\mathbf{x}}(t_{k-1})$ to the next epoch t_k using the multifidelity scheme in Section 3.4 to obtain $M_{\mathbf{x}}(t_k)$
2. Projection of $M_{\mathbf{x}}(t_k)$ onto the observables space (ρ, α, δ) as in Section 3.5 to obtain $M_{\hat{\mathbf{y}}}(t_k)$
3. Pruning of $M_{\hat{\mathbf{y}}}(t_k)$ and $M_{\mathbf{x}}(t_k)$ with information from (α_k, δ_k) as in Section 3.6 to obtain the reduced manifolds $M'_{\hat{\mathbf{y}}}(t_k), M'_{\mathbf{x}}(t_k)$ as well as isolate potential outliers. If an outlier is found, no pruning is performed and $M'_{\mathbf{x}}(t_k)$ coincides with $M_{\mathbf{x}}(t_k)$
4. Merging of the domains in $M'_{\mathbf{x}}(t_k)$ as in Section 2.5 since nonlinearities are weaker in orbital elements space than in (ρ, α, δ) and fewer domains are thus required to accurately capture the uncertainty in this space

The procedure thus ends at epoch t_M with the computation of $M'_{\hat{\mathbf{y}}}(t_M)$ and $M'_{\hat{\mathbf{x}}}(t_M)$ for the last available measurement. A list of indexes k corresponding to detected outliers is also available at this stage.

3.8 Batch orbit determination algorithms

Solving the batch OD problem requires to find an estimate of the orbit state $\hat{\mathbf{x}}_0 = \hat{\mathbf{x}}(t_0)$, at some reference epoch t_0 , that minimizes the residuals between the real observations $(\mathbf{y}_k)_{k=1}^m$ collected at epochs $(t_k)_{k=1}^m$ and belonging to some observation space $\mathbf{Y} \subseteq \mathbb{R}^p$, and the expected (or theoretical) measurements $(\hat{\mathbf{y}}_k)_{k=1}^m$. The latter are computed by propagating $\hat{\mathbf{x}}_0$ to t_k and projecting the state $\hat{\mathbf{x}}_k$ onto the observable space, i.e.,

$$\hat{\mathbf{y}}_k = \mathbf{h}_k(\hat{\mathbf{x}}_k) \quad k \in [1, m] \quad (28)$$

where \mathbf{h}_k is the observation function at epoch t_k . Assuming that the estimated state $\hat{\mathbf{x}}_k$ is close to the true object's state \mathbf{x}_k at epoch t_k , \mathbf{h}_k can be linearized using a Taylor expansion as

$$\begin{aligned} \mathbf{h}_k(\mathbf{x}_k) &\approx \mathbf{h}_k(\hat{\mathbf{x}}_k) + \tilde{H}_k \delta \mathbf{x}_k \\ &\approx \mathbf{h}_k(\hat{\mathbf{x}}_k) + \tilde{H}_k \Phi(t_k, t_0) \delta \mathbf{x}_0 \\ &\approx \mathbf{h}_k(\hat{\mathbf{x}}_k) + H_k \delta \mathbf{x}_0 \end{aligned} \quad (29)$$

with $\Phi(t_k, t_0)$ the state transition matrix (STM) from t_0 to t_k , and \tilde{H}_k the partials of \mathbf{h}_k with respect to \mathbf{x}_k and evaluated at $\hat{\mathbf{x}}_k$ given by

$$\tilde{H}_k = \left. \frac{\partial \mathbf{h}_k}{\partial \mathbf{x}_k} \right|_{\hat{\mathbf{x}}_k} \quad (30)$$

In this work, DA is leveraged to automate the computation of both $\hat{\mathbf{y}}_k$ and H_k . More specifically, $\hat{\mathbf{x}}_0$ is firstly initialized as the DA vector $[\hat{\mathbf{x}}_0] = \hat{\mathbf{x}}_0 + \delta \mathbf{x}_0$ and all operations are carried out in the DA framework after setting the expansion order equal to one. The Taylor expansion of $\hat{\mathbf{y}}_k$ at each epoch is thus available as

$$[\hat{\mathbf{y}}_k] = \mathcal{T}_{\hat{\mathbf{y}}_k}(\delta \mathbf{x}_0) \quad (31)$$

$\mathbf{h}_k(\hat{\mathbf{x}}_k)$ and H_k are then retrieved as the constant part and the linear part of Eq. (31), respectively. This avoids the needs for an analytical expression of $\partial \mathbf{h}_k / \partial \mathbf{x}_k$ and the integration of the 6×6 variational equations for Φ . The residuals are then readily computed as

$$\begin{aligned} \mathbf{e} &= \tilde{\mathbf{y}} - \hat{\mathbf{y}} \\ &= \tilde{\mathbf{y}} - \mathbf{h}(\hat{\mathbf{x}}) - H \delta \mathbf{x}_0 \\ &= \Delta \mathbf{y} - H \delta \mathbf{x}_0 \end{aligned} \quad (32)$$

where the total observations vectors and Jacobian are defined as

$$\tilde{\mathbf{y}} = [\tilde{\mathbf{y}}_1^T, \dots, \tilde{\mathbf{y}}_m^T]^T \quad (33a)$$

$$\hat{\mathbf{y}} = [\hat{\mathbf{y}}_1^T, \dots, \hat{\mathbf{y}}_m^T]^T \quad (33b)$$

$$\mathbf{h}(\hat{\mathbf{x}}) = [\mathbf{h}_1(\hat{\mathbf{x}}_1), \dots, \mathbf{h}_k(\hat{\mathbf{x}}_k)]^T \quad (33c)$$

$$H = [H_1^T, \dots, H_m^T]^T \quad (33d)$$

The three vectors $\tilde{\mathbf{y}}$, $\hat{\mathbf{y}}$ and $\mathbf{h}(\hat{\mathbf{x}})$ have size $mp \times 1$ while the matrix H has size $mp \times n$, where n is the dimension of $\hat{\mathbf{x}}_k$.

Given an initial guess for $\hat{\mathbf{x}}_0$ denoted as $\hat{\mathbf{x}}_0^0$, the objective of the OD algorithm is to iteratively solve for $\delta\mathbf{x}_0$ and compute an updated estimate $\hat{\mathbf{x}}_0^j$ as

$$\hat{\mathbf{x}}_0^j = \hat{\mathbf{x}}_0^{j-1} + \delta\mathbf{x}_0 \quad (34)$$

with j iteration number. The recursive procedure terminates as soon as one of the following criteria is satisfied

- $\|\hat{\mathbf{y}}^j - \hat{\mathbf{y}}^{j-1}\|_2 < \varepsilon_{res}$, i.e. the residuals at two subsequent iterations differ by less than the residual tolerance ε_{res} .
- $|J^j - J^{j-1}| < \varepsilon_{opt}$, i.e. the cost functions at two subsequent iterations differ by less than the optimality tolerance ε_{opt} .¹
- $\|\delta\hat{\mathbf{x}}_0\|_2 < \varepsilon_{step}$, i.e. the state update is smaller than the step tolerance ε_{step} .
- $j = j_{max}$, i.e. a maximum number of iterations has been reached.

3.8.1 Least squares

The LS solution to the OD problem solves for $\delta\mathbf{x}_0$ that minimizes the residuals in the LS sense. The cost function is given by

$$J_{LS} = \frac{1}{2} \mathbf{e}^T W \mathbf{e} = \frac{1}{2} [\Delta\mathbf{y} - H\delta\mathbf{x}_0]^T W [\Delta\mathbf{y} - H\delta\mathbf{x}_0] \quad (35)$$

with $W = \text{diag}(1/\sigma_i^2)$ the diagonal weight matrix where σ_i is the sensor noise standard deviation corresponding to the i^{th} observation. The state update that minimizes Eq. (35) is obtained using the Levenberg–Marquardt (LM) algorithm [25] (damped LS) as

$$\delta\mathbf{x}_0 = (H^T W H + \lambda I)^{-1} H^T W \Delta\mathbf{y} \quad (36)$$

with λ the damping parameter and I the identity matrix. The covariance matrix of $\hat{\mathbf{x}}_0$ is finally estimated as

$$P_0 = (H^T W H)^{-1} \quad (37)$$

¹the cost function J is defined in Sections 3.8.1 and 3.8.2.

3.8.2 Least sum of absolute residuals

The LSAR solution to the OD problem was proposed in [11] as an alternative to LS optimization capable of rejecting outlier measurements in the presence of redundant observations. The cost function to be minimized is

$$J_{LSAR} = \sum_{i=1}^{mp} \tilde{w}_i |e_i| \quad (38)$$

with e_i the components of \mathbf{e} and \tilde{w}_i the weights defined as $\tilde{w}_i = 1/(1.24\sigma_i)$ [26]. The problem is recast as a linear programming problem (LPP) in the form

$$\min_{\mathbf{z}} \mathbf{c}^T \mathbf{z} \quad \text{subject to } Q\mathbf{z} \leq \mathbf{k} \quad (39)$$

with

$$Q = \begin{bmatrix} -H & -I_{mp \times mp} \\ H & -I_{mp \times mp} \end{bmatrix} \quad (40a)$$

$$\mathbf{z} = [\delta \mathbf{x}_0^T \quad \mathbf{s}^T]^T \quad (40b)$$

$$\mathbf{k} = [-\Delta \mathbf{y}^T \quad \Delta \mathbf{y}^T]^T \quad (40c)$$

$$\mathbf{c} = [\mathbf{0}_{6 \times 1}^T \quad \tilde{\mathbf{w}}^T]^T \quad (40d)$$

and \mathbf{s} slack variables for the constraint vector \mathbf{e} such that

$$|e_i| \leq s_i \quad i = 1, \dots, mp \quad (41)$$

Throughout this work, the solver MOSEK² with its interior point algorithm is used to efficiently solve Eq. (39). The covariance matrix of $\hat{\mathbf{x}}_0$ is then estimated as

$$\tilde{P}_0 = (H^T \tilde{W} H)^{-1} \quad (42)$$

with $\tilde{W} = \text{diag}(\tilde{w}_i^2) = W/1.24^2$.

²<https://www.mosek.com>

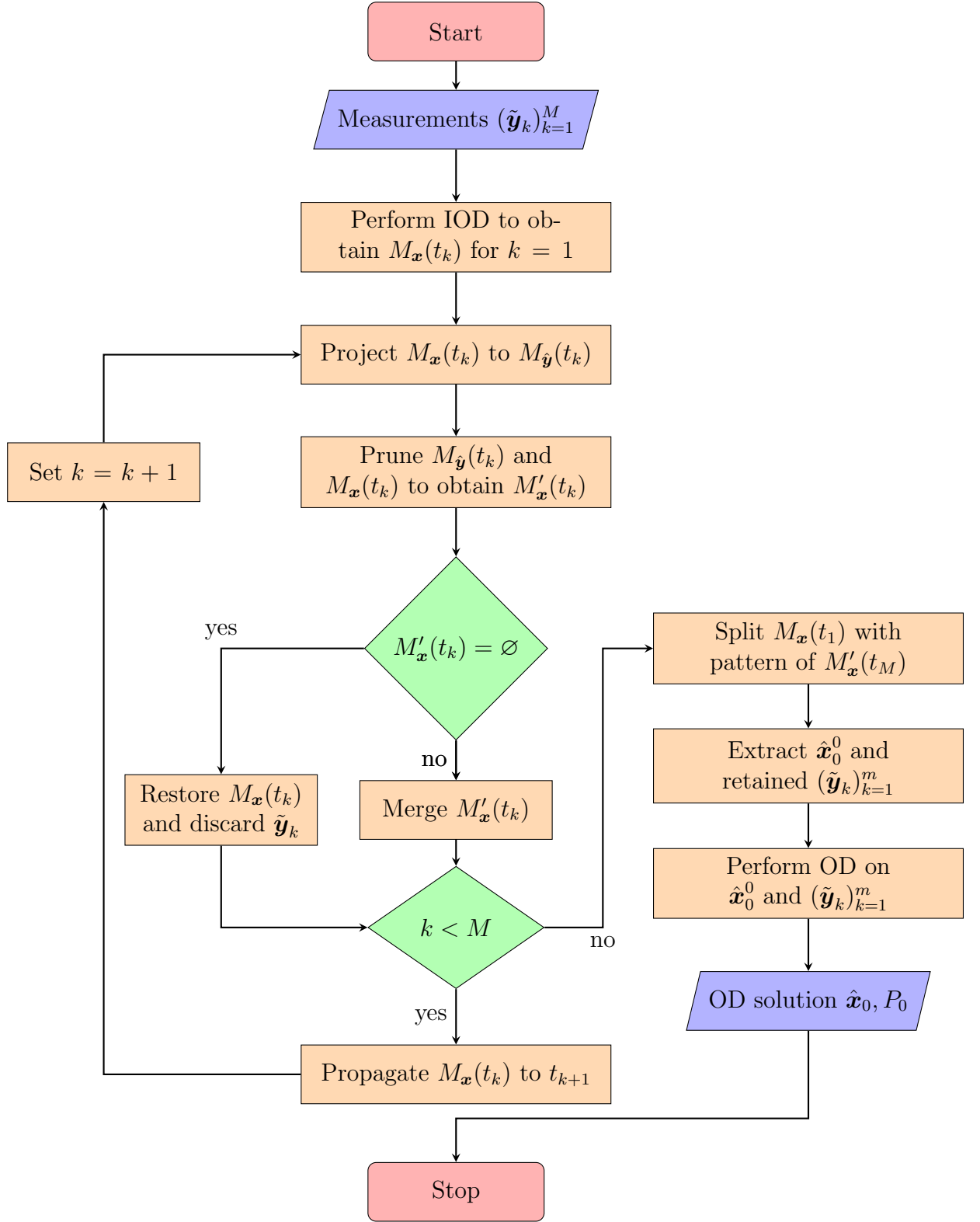


Figure 1: Workflow of the proposed robust OD solution

4 Numerical Application

This section presents an application of the developed algorithm in real operational scenarios. The selected object is the rocket body of an Ariane 44L launched in 2002 and catalogued with NORAD ID 27402. This object is on a geostationary transfer orbit (GTO) with semi-major axis of about 23 000 km and inclination of 3.9°, and is regularly tracked by the optical telescopes of the TAROT network [27]. Two analyses are conducted to highlight different aspects of the proposed tool. In both cases, two objects are considered: the one of interest (the target), and a third-party one (the outlier). The outlier is simulated, and noised measurements are produced out of it to simulate observations that should not be associated to the target object. Instead, the observations that should be associated to the SO of interest are either generated from a synthetic trajectory in Section 4.1 or drawn from real observations in Section 4.2. Both analyses consider a time span of about five days that includes five passages of the SOs over the two telescopes in La Reunion and Calern (France). Passages epochs, duration and number of measurements are summarized in Table 1.

Sensor	Epoch (UTC)	Duration	#measurements
La Reunion	2019-02-25T18:49:01.148	05:13:10.189	8
La Reunion	2019-02-27T23:27:20.511	00:00:48.972	3
La Reunion	2019-03-01T01:35:55.561	00:00:48.019	3
La Reunion	2019-03-01T23:10:59.277	00:00:24.011	2
Calern	2019-03-01T23:58:27.006	00:00:24.926	2

Table 1: Epoch, duration and number of measurements for the considered passages

Throughout these analyses, the analytical SGP4 propagator [20] is used as low-fidelity dynamical model while an high-fidelity numerical propagator is set up with the following force models

- Earth’s gravity potential modeled with spherical harmonics truncated at order/degree 16 [28]
- Sun and Moon third-body attraction with bodies’ position from JPL DE440 ephemerides [29]
- Atmospheric drag with Harris-Priester atmosphere model [30]
- SRP with cylindrical Earth’s shadow model [31]

The algorithms were coded in Java and make use of the CNES’s own DA engine PACE (Polynomial Algebra Computational Engine) largely extended by the authors. The code interfaces with Orekit³ for standard flight dynamics routines (SGP4 propagator, force models, time scales and reference frames conversions) and uses the Hipparchus⁴ implementation of the 8(5,3) Dormand-Prince numerical integrator and LM optimizer. The MOSEK solver is interfaced through its Fusion API for Java⁵. All simulations were run on a Dell Precision 3541 equipped with an Intel[®] Core™ i5-9400H @ 2.50 GHz and 16GB of RAM running Ubuntu 20.04 LTS.

4.1 Synthetic measurements

The first analysis uses synthetic measurements for both objects, so as a true reference trajectory is available to assess the algorithm’s performance. For the target SO an assumed true state is retrieved from TLE data. The outlier orbit is then obtained by perturbing the target’s eccentricity by $\Delta e = -0.02$. The Keplerian parameters at epoch are given in Table 2 for both SOs. The trajectories of the two objects are simulated using the high-fidelity propagator and synthetic measurements are drawn from them. These are then corrupted with a zero-mean Gaussian noise with standard deviations $\sigma_\alpha = 1.285''$ and $\sigma_\delta = 1.280''$ to simulate sensor noise. Four different scenarios are then analyzed as listed in Table 3. In scenario A and B only correlated measurements are processed. Observations associated to the outlier are then added in scenarios C and D.

	a , km	e , -	i , °	ω , °	Ω , °	M_0 , °
Target	22 953.853	0.708	3.388	172.980	-168.891	60.743
Outlier	22 953.853	0.688	3.388	172.980	-168.891	60.743

Table 2: Initial conditions for target and outlier orbits

The IOD algorithm described in Section 3.2 is run on the first passage and the estimated state at t_0 used to initialize the pruning scheme. In this case, the LOADS algorithm generates a single domain and thus $M_{\mathbf{x}} = \{\{\mathbf{x}_0\}\}$. In scenarios B and D this manifold is then propagated to the latest epoch using the algorithm in Section 3.7. The evolution over time of the number of domains is summarized in Tables 4 and 5 respectively. A visual representation is also given in Figs. 2 and 3. In this pictures, orange squares and yellow crosses correspond to the size of

³<https://www.orekit.org/>

⁴<https://hipparchus.org/>

⁵<https://docs.mosek.com/latest/javafusion/index.html>

Scenario #	Pruning	Outliers
A	NO	NO
B	YES	NO
C	NO	3 rd passage
D	YES	3 rd passage

Table 3: Test case scenarios with simulated measurements

the osculating elements manifolds after propagation (step #1) and merging (step #4). Blue diamonds and green plus signs correspond to the size of the observables manifolds after projection (step #2) and pruning (step #3). Vertical dashed lines correspond to the observations epochs.

Time since t_0 , h	Number of domains			
	#1 Propagation	#2 Projection	#3 Pruning	#4 Merging
0	1	1	1	1
0.007	1	1	1	1
0.013	1	1	1	1
4.393	1	1	1	1
4.400	1	1	1	1
5.206	1	1	1	1
5.213	1	1	1	1
5.219	1	1	1	1
52.639	1	9	7	5
52.645	5	7	7	5
52.652	5	7	7	5
78.782	5	21	17	11
78.788	11	17	17	11
78.795	11	17	17	11
100.366	11	51	38	18
100.373	18	38	38	18
101.157	18	38	35	19
101.164	19	35	35	19

Table 4: Number of domains as function of propagation time for scenario B

The effectiveness of the pruning algorithm is clearly seen by comparing, for the same epoch, the number of domains after steps #2 and #3. It is also noted that the merging step is key to limit the number of domains processed in step #1. If not

Number of domains				
Time since t_0 , h	#1 Propagation	#2 Projection	#3 Pruning	#4 Merging
0	1	1	1	1
0.007	1	1	1	1
0.013	1	1	1	1
4.393	1	1	1	1
4.400	1	1	1	1
5.206	1	1	1	1
5.213	1	1	1	1
5.219	1	1	1	1
52.639	1	9	7	5
52.645	5	7	7	5
52.652	5	7	7	5
78.782	5	21	21	5
78.788	5	21	21	5
78.795	5	21	21	5
100.366	5	63	38	18
100.373	18	38	38	18
101.157	18	38	35	19
101.164	19	35	35	19

Table 5: Number of domains as function of propagation time for scenario D

performed, the propagation algorithm will enter the next iteration with a number of domains corresponding to the third column (or green plus signs) rather than the fourth one (or yellow crosses). The effectiveness of the selected state representation in limiting the number of domains generated during propagation is also demonstrated. All splits are in fact triggered by the projection onto the observables space and the increased number of domains to be propagated in subsequent steps is the result of an imperfect merging during step #4. Since domains are discarded in step #3, several incomplete triplets are found by the merging scheme which thus fails to recombine the polynomials as they were before step #2. The correct detection of outliers is then demonstrated in Table 5, where no modification of the domains occur in the third measurement block which corresponds to uncorrelated measurements. In this case, the algorithm correctly detects the outliers and does not prune the projected manifold. Moreover, the high-fidelity correction is key in this step, since using only SGP4 for the propagation would have produced a number of false outliers.

An example of pruning is presented in Fig. 4 where the estimated bounds for

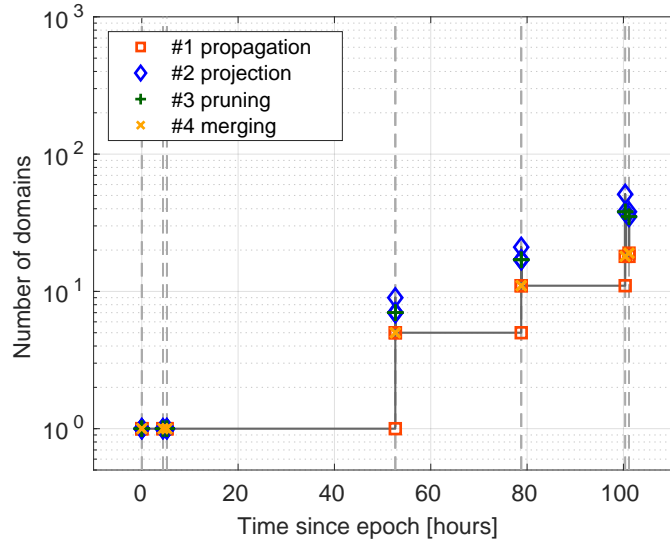


Figure 2: Number of domains as function of propagation time for scenario B

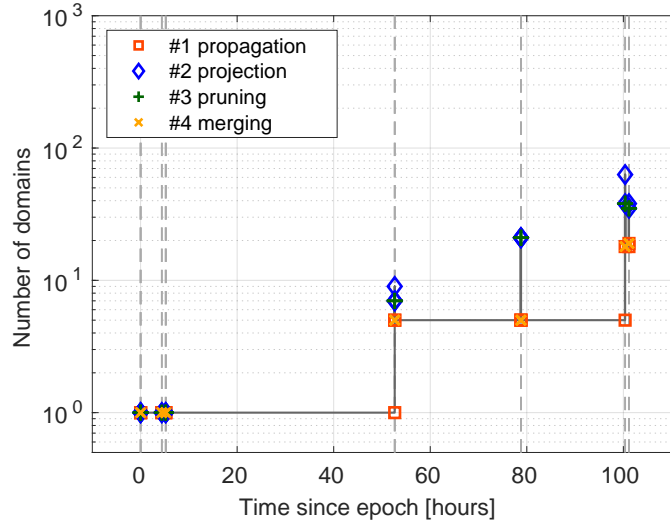


Figure 3: Number of domains as function of propagation time for scenario D

both $M_{\hat{y}}(t_k)$ (gray boxes) and $M'_{\hat{y}}(t_k)$ (gold boxes) are plotted in (α, δ) space. The large overlap between gold boxes is an indicator that most of the uncertainty is on the LOS distance which cannot be observed with optical telescopes. Still, the pruning algorithm is highly effective in reducing the uncertainty on the observed quantities. This is demonstrated also in Fig. 5 which represents the uncertainty on the IOD solution in (δ_2, δ_3) space. The gray box identifies the edges of the initial domain which corresponds to the uncertainty on the measurements. Instead, the golden boxes are the edges of the domains that maps into the solution manifold

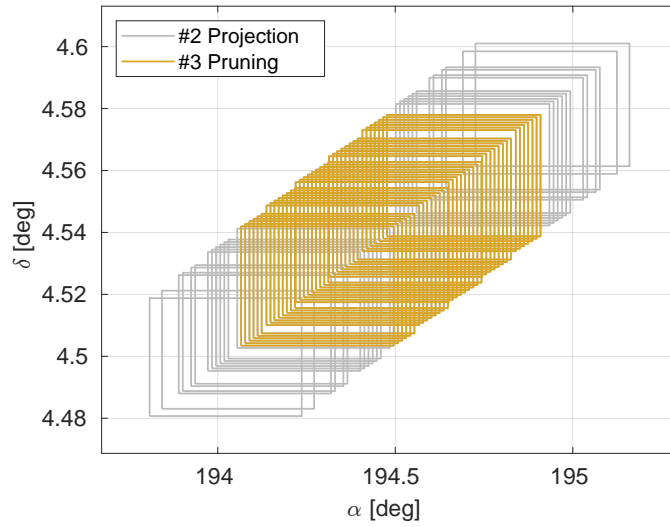


Figure 4: Estimated bounds of projected and pruned domains at 100.366 h after t_0 for scenario D

at the last epoch. It is thus seen the effectiveness of the algorithm in tightening the bounds on the initial estimate as the propagation steps forward and more information is exploited to refine the IOD solution.

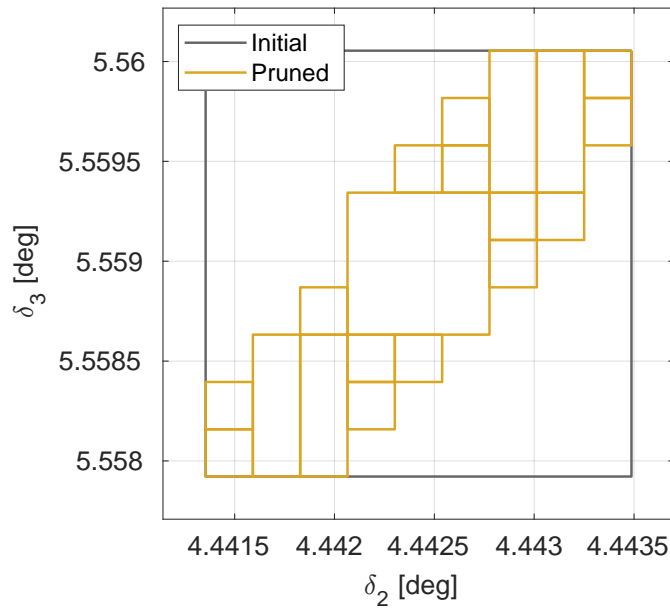


Figure 5: Edges of the initial and pruned IOD solution in (δ_2, δ_3) space for scenario D

OD is then performed for all scenarios comparing the performance of the LS and LSAR algorithms introduced in Section 3.8. The true cartesian state of the target object and the IOD solution used to initialize the OD routines are given in Table 6. The resulting estimation errors and $\pm 3\sigma$ bounds are summarized in Tables 7 to 9 for scenarios A and B, C and D respectively.

	x , km	y , km	z , km	v_x , km s ⁻¹	v_y , km s ⁻¹	v_z , km s ⁻¹
True	-2.15512×10^4	1.44049×10^4	-1.08246×10^3	-3.58040	-7.36465×10^{-1}	1.94379×10^{-3}
Guess	-2.15536×10^4	1.44061×10^4	-1.08236×10^3	-3.57995	-7.36567×10^{-1}	1.92179×10^{-3}

Table 6: True state and initial guess for scenarios A to D

Table 7 corresponds to the two scenarios with no outliers in which the pruning algorithm has no effect on the final solution. Both algorithms provide a consistent estimate of the SO state converging in just three iterations. As expected, the LS solution is characterized by tighter bounds on the states since the algorithm is the minimum variance estimator for a model with zero-mean Gaussian noise distribution [11].

	x , km	y , km	z , km	v_x , km s ⁻¹	v_y , km s ⁻¹	v_z , km s ⁻¹
LS Error	-1.406×10^{-3}	-1.663×10^{-1}	6.405×10^{-2}	-1.437×10^{-5}	-6.954×10^{-6}	-8.220×10^{-7}
$\pm 3\sigma$ bounds	9.118×10^{-1}	4.564×10^{-1}	2.053×10^{-1}	1.710×10^{-4}	4.022×10^{-5}	1.535×10^{-5}
LSAR Error	-1.796×10^{-1}	-8.256×10^{-2}	4.507×10^{-2}	1.892×10^{-5}	-1.060×10^{-5}	-2.115×10^{-7}
$\pm 3\sigma$ bounds	1.131	5.659×10^{-1}	2.546×10^{-1}	2.120×10^{-4}	4.987×10^{-5}	1.903×10^{-5}

Table 7: LS and LSAR estimation errors and $\pm 3\sigma$ bounds for scenario A and B

The effects of measurement outliers on the estimated state is then shown in Table 7. With no measurement preprocessing, the LS estimator fails to converge to the true solution and returns an estimate characterized by large errors in both position (≈ 700 km) and velocity (≈ 0.12 km s⁻¹) converging in nine iterations. On the contrary, the LSAR algorithm is capable of rejecting the outliers and still converging to the true solution at the expenses of a longer runtime (six iterations vs three in scenarios A and B).

The accuracy of the LS estimate is then restored in scenario D in which outliers have been detected and discarded by the pruning scheme. Results in Table 9 are in fact similar to those in Table 7 and the LS estimation is again characterized by tighter bounds on the states. The LSAR algorithm also benefits from measurements preprocessing since excluding the uncorrelated observations from the processed ones reduces the number of iterations from six to just two. Given that

	x , km	y , km	z , km	v_x , km s ⁻¹	v_y , km s ⁻¹	v_z , km s ⁻¹
LS Error	-5.791×10^2	3.775×10^2	3.448×10^1	1.181×10^{-1}	-2.462×10^{-2}	2.569×10^{-3}
$\pm 3\sigma$ bounds	8.620×10^{-1}	4.224×10^{-1}	2.100×10^{-1}	1.573×10^{-4}	3.680×10^{-5}	1.473×10^{-5}
LSAR Error	-7.726×10^{-1}	2.574×10^{-1}	-1.491×10^{-2}	1.384×10^{-4}	-4.155×10^{-5}	-3.414×10^{-7}
$\pm 3\sigma$ bounds	1.131	5.658×10^{-1}	2.546×10^{-1}	2.120×10^{-4}	4.987×10^{-5}	1.903×10^{-5}

Table 8: LS and LSAR estimation errors and $\pm 3\sigma$ bounds for scenario C

the runtime of the pruning algorithm is comparable with that of a single iteration of the LSAR routine, the total runtime is about 43% of that of scenario C.

	x , km	y , km	z , km	v_x , km s ⁻¹	v_y , km s ⁻¹	v_z , km s ⁻¹
LS Error	-1.887×10^{-1}	-4.353×10^{-2}	4.404×10^{-2}	2.450×10^{-5}	-1.513×10^{-5}	-2.041×10^{-6}
$\pm 3\sigma$ bounds	1.096	5.982×10^{-1}	2.265×10^{-1}	2.114×10^{-4}	4.795×10^{-5}	1.679×10^{-5}
LSAR Error	-3.337×10^{-1}	5.742×10^{-3}	5.557×10^{-2}	4.971×10^{-5}	-1.859×10^{-5}	4.287×10^{-7}
$\pm 3\sigma$ bounds	1.359	7.417×10^{-1}	2.808×10^{-1}	2.622×10^{-4}	5.946×10^{-5}	2.082×10^{-5}

Table 9: LS and LSAR estimation errors and $\pm 3\sigma$ bounds for scenario D

4.2 TAROT measurements

The second analysis uses real observation data from the TAROT network to estimate the target SO state. Synthetic measurements for the outlier orbit generated in Section 4.1 are still used to corrupt the available data and assess the robustness of the proposed tool. The four scenarios presented in Section 4.1 are reproduced here as summarized in Table 10. To account for the unknown forces acting on the SOs, stochastic accelerations modeled as additive white Gaussian noise are included in the high-fidelity dynamics. Their effect is taken into account by the pruning scheme using the SNC algorithm described in Section 3.3. A deterministic dynamics is instead used for the subsequent batch OD.

The IOD algorithm run on the first passage still return a single domain which is then used to initialize the sequential pruning in scenarios F and H. The time evolution of the number of domains is summarized in Tables 11 and 12 and depicted in Figs. 6 and 7 respectively for the two scenarios. The immediate effect of stochastic accelerations can be identified in the larger number of domains generated during the projection (#2) step. Indeed, integrating the uncertainty due to these perturbations results in an inflated covariance for the prior states which, in turns, triggers more splits when projected onto the observables space. At the same

Case #	Pruning	Outliers
E	NO	NO
F	YES	NO
G	NO	3 rd passage
H	YES	3 rd passage

Table 10: Test case scenarios with real measurements from the TAROT network

time, the pruning scheme is even more effective and the ratio between projected and retained domains is higher in Table 11 than in Table 4. Overall, the characteristics analyzed in Section 4.1 are recovered also in these scenarios, including the correct detection of uncorrelated measurements and the needs for an high-fidelity correction of the low-fidelity solution to maintain a consistent estimate.

Time since t_0 , h	Number of domains			
	#1 Propagation	#2 Projection	#3 Pruning	#4 Merging
0	1	1	1	1
0.007	1	1	1	1
0.013	1	1	1	1
4.393	1	1	1	1
4.400	1	1	1	1
5.206	1	1	1	1
5.213	1	1	1	1
5.219	1	1	1	1
52.639	1	3	3	1
52.645	1	3	3	1
52.652	1	3	3	1
78.782	1	243	84	40
78.788	40	84	81	41
78.795	41	81	81	41
100.366	41	243	169	63
100.373	63	169	168	66
101.157	66	168	118	52
101.164	52	118	115	49

Table 11: Number of domains as function of propagation time for scenario F

Two examples of pruning are depicted in Figs. 8 and 9 for scenarios F and H respectively. These correspond to the epochs with the highest ratio of projected

Number of domains				
Time since t_0 , h	#1 Propagation	#2 Projection	#3 Pruning	#4 Merging
0	1	1	1	1
0.007	1	1	1	1
0.013	1	1	1	1
4.393	1	1	1	1
4.400	1	1	1	1
5.206	1	1	1	1
5.213	1	1	1	1
5.219	1	1	1	1
52.639	1	3	3	1
52.645	1	3	3	1
52.652	1	3	3	1
78.782	1	243	243	1
78.788	1	243	243	1
78.795	1	243	243	1
100.366	1	729	205	77
100.373	77	205	205	77
101.157	77	205	189	77
101.164	77	189	187	75

Table 12: Number of domains as function of propagation time for scenario H

over retained domains, i.e. when the largest number of domains is dropped and the uncertainty is reduced the most. As expected, for scenario H this occurs at the first measurements after the block of outliers which ends a long propagation arc without useful information to reduce the growing uncertainty (since uncorrelated measurements are ignored).

The uncertainty on the IOD solution for the two scenarios is depicted in Figs. 10 and 11 in which a projection of the initial (gray box) and pruned domains (golden boxes) onto the (α_2, δ_2) space is shown. A comparison of the area covered by the golden boxes demonstrates that for both scenarios the correct subregion of the initial domain that contains the true measurement is identified. The main difference is found in the choice of the splitting direction, as seen by comparing the shape of the small boxes that constitutes the refined solution. In Fig. 10 these are mostly square domains and indicate an almost even allocation of splits along the two directions. On the contrary, Fig. 11 is characterized by a single split along the δ_2 variable resulting in more elongated rectangular domains.

Similarly to Section 4.1, OD is performed in the four scenarios to assess the

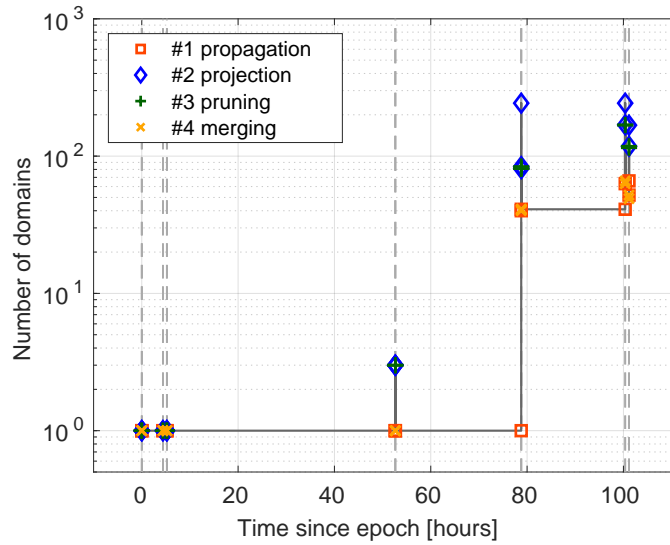


Figure 6: Number of domains as function of propagation time for scenario F

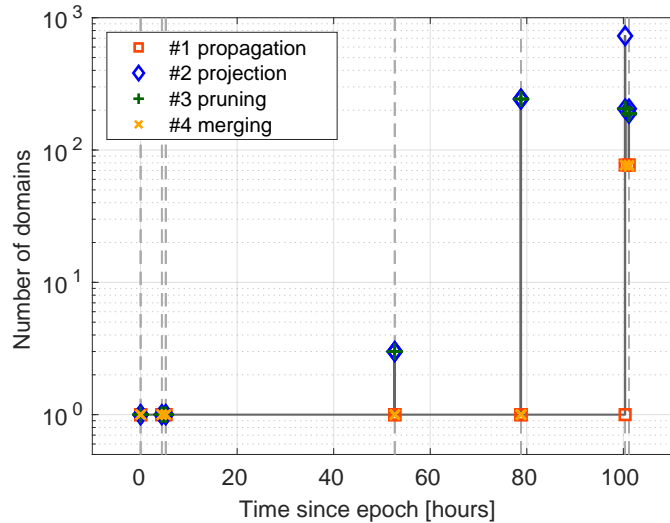


Figure 7: Number of domains as function of propagation time for scenario H

performance of the LS and LSAR estimators while processing both raw and pruned observations. The true state is not available in this case, and the best estimate available from a third-party solution to the OD problem is used instead. Given the dynamical model and parameters used to obtain such estimate are unknown, errors in the order of 10 km and 0.001 km s^{-1} over a five days time span are considered acceptable in this case. The aforementioned reference solution is thus reported in Table 13 together with the initial guesses provided to the batch estimators. The lasts coincide with the raw IOD solution for scenarios E and G (since no pruning

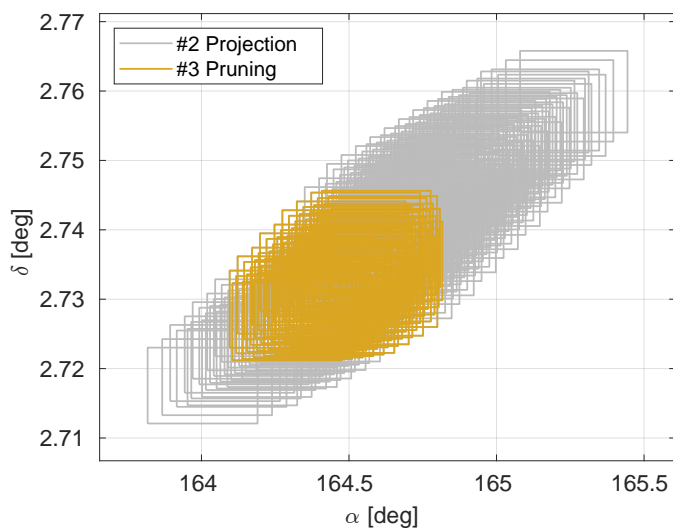


Figure 8: Estimated bounds of projected and pruned domains at 78.782 h after t_0 for scenario F

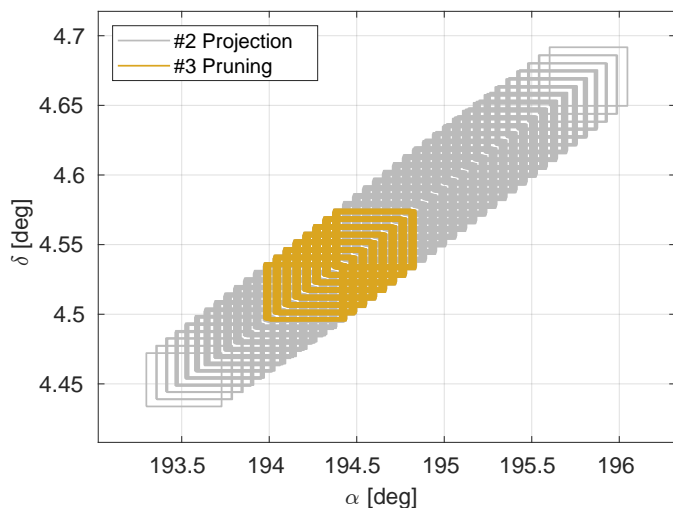


Figure 9: Estimated bounds of projected and pruned domains at 100.366 h after t_0 for scenario H

is performed) and to the domain that is characterized by the smallest residuals among the pruned ones for scenarios F and H.

Table 14 reports the LS and LSAR estimation errors and $\pm 3\sigma$ bounds for scenario E. These are qualitatively identical to those of scenario F which are omitted for conciseness. The LS solution is again characterized by tighter bounds on the states, even though the errors with respect to the assumed reference are larger than for the LSAR estimate. In this case, five iterations are needed for the LS

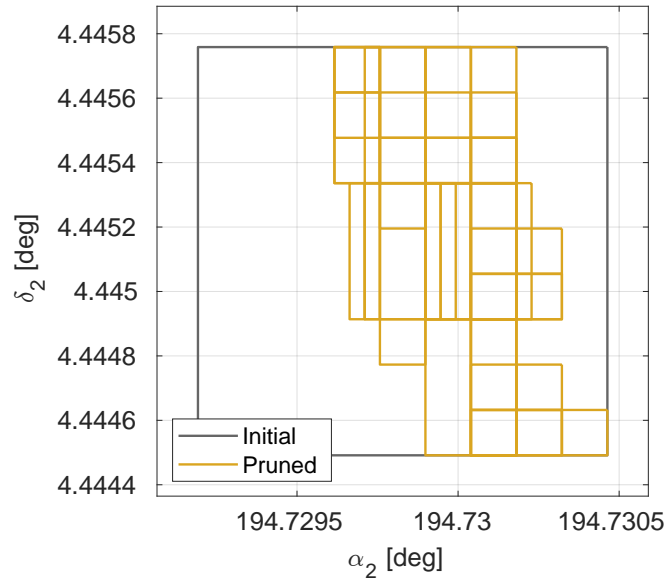


Figure 10: Edges of the initial and pruned IOD solution in (α_2, δ_2) space for scenario F

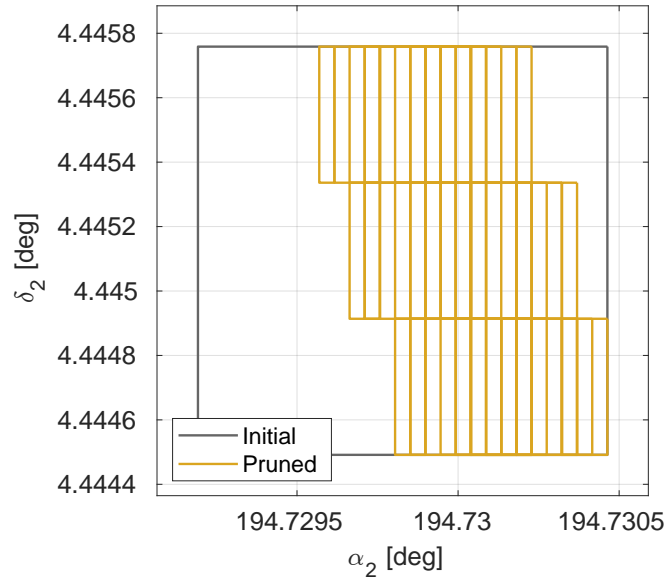


Figure 11: Edges of the initial and pruned IOD solution in (α_2, δ_2) space for scenario H

estimator to converge while only three are required by the LSAR counterpart. These numbers are downed to three and two respectively in scenario F in which the algorithms are initialized with the refined IOD solution. The lower number of

	x , km	y , km	z , km	v_x , km s ⁻¹	v_y , km s ⁻¹	v_z , km s ⁻¹
True	-2.15512×10^4	1.44049×10^4	-1.08246×10^3	-3.58040	-7.36465×10^{-1}	1.94379×10^{-3}
Guess E	-2.15471×10^4	1.44047×10^4	-1.08199×10^3	-3.58086	-7.35900×10^{-1}	2.00492×10^{-3}
Guess F	-2.15547×10^4	1.44090×10^4	-1.08147×10^3	-3.57970	-7.36564×10^{-1}	2.12008×10^{-3}
Guess G	-2.15471×10^4	1.44047×10^4	-1.08199×10^3	-3.58086	-7.35900×10^{-1}	2.00492×10^{-3}
Guess H	-2.15499×10^4	1.44063×10^4	-1.08180×10^3	-3.58044	-7.36163×10^{-1}	2.04241×10^{-3}

Table 13: True state and initial guesses for scenarios E to H

iterations results in a 20% smaller runtime for the LS solution while no improvement is observed for the LSAR one.

	x , km	y , km	z , km	v_x , km s ⁻¹	v_y , km s ⁻¹	v_z , km s ⁻¹
LS Error	9.185	-3.275	1.198×10^{-1}	-1.742×10^{-3}	3.041×10^{-4}	1.367×10^{-4}
$\pm 3\sigma$ bounds	7.809×10^{-1}	4.144×10^{-1}	1.387×10^{-1}	1.503×10^{-4}	3.300×10^{-5}	1.085×10^{-5}
LSAR Error	-6.023×10^{-1}	2.324	7.749×10^{-1}	1.832×10^{-4}	7.608×10^{-5}	1.710×10^{-4}
$\pm 3\sigma$ bounds	9.669×10^{-1}	5.129×10^{-1}	1.720×10^{-1}	1.860×10^{-4}	4.085×10^{-5}	1.344×10^{-5}

Table 14: LS and LSAR estimation errors and $\pm 3\sigma$ bounds for scenario E

The effects of measurements outliers among the processed set is then shown in Table 15 which summarizes the results obtained for scenario G. In this case, six and three iterations are needed by the LS and LSAR algorithms to converge. As for scenario C, the LS estimate exhibits large errors in both positions (≈ 550 km) and velocity (≈ 0.1 km s⁻¹) thus supporting the needs for a preprocessing algorithm capable of detecting and isolating uncorrelated observations. On the contrary, the LSAR scheme shows an excellent performance that matches the one of scenario H reported in Table 16. Differently from Section 4.1, no reduction in the number of iterations is observed when processing correlated measurements only instead of the entire available set. The inclusion of the pruning step is however paramount to restore the accuracy of the LS estimate as demonstrated in Table 16. In this case a consistent estimate is in fact obtained and the LS estimator converges in just three iterations and a 33% smaller total runtime compared to scenario G.

5 Conclusions

A pruning algorithm for the refinement of an IOD solution and the detection of measurement outliers was presented. This scheme is broken down into four main

	x , km	y , km	z , km	v_x , km s ⁻¹	v_y , km s ⁻¹	v_z , km s ⁻¹
LS Error	-4.646×10^2	2.896×10^2	3.166×10^1	9.377×10^{-2}	-2.053×10^{-2}	1.565×10^{-3}
$\pm 3\sigma$ bounds	7.678×10^{-1}	4.096×10^{-1}	1.440×10^{-1}	1.456×10^{-4}	3.172×10^{-5}	1.070×10^{-5}
LSAR Error	-1.256	2.694	8.192×10^{-1}	2.882×10^{-4}	2.517×10^{-5}	1.802×10^{-4}
$\pm 3\sigma$ bounds	1.007	5.409×10^{-1}	1.760×10^{-1}	1.945×10^{-4}	4.270×10^{-5}	1.371×10^{-5}

Table 15: LS and LSAR estimation errors and $\pm 3\sigma$ bounds for scenario G

	x , km	y , km	z , km	v_x , km s ⁻¹	v_y , km s ⁻¹	v_z , km s ⁻¹
LS Error	3.314	3.163×10^{-1}	5.045×10^{-1}	-5.533×10^{-4}	4.362×10^{-5}	1.564×10^{-4}
$\pm 3\sigma$ bounds	9.231×10^{-1}	5.120×10^{-1}	1.496×10^{-1}	1.803×10^{-4}	3.956×10^{-5}	1.153×10^{-5}
LSAR Error	-1.121	2.618	8.129×10^{-1}	2.622×10^{-4}	3.099×10^{-5}	1.799×10^{-4}
$\pm 3\sigma$ bounds	1.144	6.348×10^{-1}	1.856×10^{-1}	2.235×10^{-4}	4.904×10^{-5}	1.430×10^{-5}

Table 16: LS and LSAR estimation errors and $\pm 3\sigma$ bounds for scenario H

steps, carried out sequentially for each available observation: propagation of the state estimate, projection onto the observables space, domains pruning based on the matching between predicted and actual measurements, and domains merging to minimize the number of trajectories to be further propagated. The uncertainty on the IOD solution is represented as a Taylor polynomial and DA techniques are leveraged to efficiently propagate the uncertainty over time. A novel splitting algorithm is also employed for the automatic control of the error committed by the truncated polynomials. To further reduce its computational effort, the prediction step is based on a bifidelity dynamical model that couples a DA-aware SGP4 propagator with an high-fidelity numerical integrator. If the first is used to map the initial uncertainty on the state to the next observation epoch, the last is employed to compute an accurate reference trajectory on which said uncertainty is centered and to include the effects of stochastic accelerations in the predicted estimate. After projecting the prior distribution onto the observables space, polynomial bounding techniques are used to estimate the range of variation of each domain and prune the ones that do not overlap with observed data at the same epoch, thus reducing the volume of the propagated uncertainty and tightening the bounds on the initial IOD solution. Measurements outliers are also detected in this step if no intersection between predicted and actual measurements is found. This algorithm is then employed as a preprocessing scheme to filter the information used by subsequent batch OD tools. Its performance is demonstrated for a GTO object using synthetic as well as real observation data from the TAROT network. It is

verified to greatly improve the accuracy of LS estimates, notoriously affected by the presence of outliers among the processed observations, and to reduce the runtime of LSAR estimators, which converge in less iterations if processing correlated measurements only instead of the entire available set.

Acknowledgments

This work is co-funded by the CNES through A. Fossà PhD program, and made use of the CNES orbital propagation tools, including the PACE library. The authors gratefully acknowledge Dr. Laura Pirovano for her support during the implementation and validation of the IOD algorithm.

References

- [1] Ryan S. Park and Daniel J. Scheeres. “Nonlinear Mapping of Gaussian Statistics: Theory and Applications to Spacecraft Trajectory Design”. In: *Journal of Guidance, Control, and Dynamics* 29.6 (Nov. 2006), pp. 1367–1375. ISSN: 0731-5090. DOI: [10.2514/1.20177](https://doi.org/10.2514/1.20177). URL: <https://arc.aiaa.org/doi/10.2514/1.20177>.
- [2] Martin Berz. *Modern Map Methods in Particle Beam Physics*. London: Academic Press, 1999, p. 317. ISBN: 0120147505. URL: <http://bt.pa.msu.edu/cgi-bin/display.pl?name=AIEP108book>.
- [3] M. Valli et al. “Nonlinear Mapping of Uncertainties in Celestial Mechanics”. In: *Journal of Guidance, Control, and Dynamics* 36.1 (Jan. 2013), pp. 48–63. ISSN: 0731-5090. DOI: [10.2514/1.58068](https://doi.org/10.2514/1.58068). URL: <https://arc.aiaa.org/doi/10.2514/1.58068>.
- [4] S.J. Julier and J.K. Uhlmann. “Unscented Filtering and Nonlinear Estimation”. In: *Proceedings of the IEEE* 92.3 (Mar. 2004), pp. 401–422. ISSN: 0018-9219. DOI: [10.1109/JPROC.2003.823141](https://doi.org/10.1109/JPROC.2003.823141). URL: <http://ieeexplore.ieee.org/document/1271397/>.
- [5] Nagavenkat Adurthi and Puneet Singla. “Conjugate Unscented Transformation-Based Approach for Accurate Conjunction Analysis”. In: *Journal of Guidance, Control, and Dynamics* 38.9 (Sept. 2015), pp. 1642–1658. ISSN: 0731-5090. DOI: [10.2514/1.G001027](https://doi.org/10.2514/1.G001027). URL: <https://arc.aiaa.org/doi/10.2514/1.G001027>.

- [6] Brandon A. Jones, Alireza Doostan, and George H. Born. “Nonlinear Propagation of Orbit Uncertainty Using Non-Intrusive Polynomial Chaos”. In: *Journal of Guidance, Control, and Dynamics* 36.2 (Mar. 2013), pp. 430–444. ISSN: 0731-5090. DOI: [10.2514/1.57599](https://doi.org/10.2514/1.57599). URL: <https://arc.aiaa.org/doi/10.2514/1.57599>.
- [7] Ya-zhong Luo and Zhen Yang. “A review of uncertainty propagation in orbital mechanics”. In: *Progress in Aerospace Sciences* 89 (Feb. 2017), pp. 23–39. ISSN: 03760421. DOI: [10.1016/j.paerosci.2016.12.002](https://doi.org/10.1016/j.paerosci.2016.12.002). URL: <https://linkinghub.elsevier.com/retrieve/pii/S0376042116301051>.
- [8] Alexander Wittig et al. “Propagation of large uncertainty sets in orbital dynamics by automatic domain splitting”. In: *Celestial Mechanics and Dynamical Astronomy* 122.3 (July 2015), pp. 239–261. ISSN: 15729478. DOI: [10.1007/s10569-015-9618-3](https://doi.org/10.1007/s10569-015-9618-3). URL: <http://link.springer.com/10.1007/s10569-015-9618-3>.
- [9] Brandon A. Jones and Ryan Weisman. “Multi-fidelity orbit uncertainty propagation”. In: *Acta Astronautica* 155 (Feb. 2019), pp. 406–417. ISSN: 00945765. DOI: [10.1016/j.actaastro.2018.10.023](https://doi.org/10.1016/j.actaastro.2018.10.023). URL: <https://linkinghub.elsevier.com/retrieve/pii/S0094576518304806>.
- [10] Alberto Fossà et al. “Multifidelity Orbit Uncertainty Propagation using Taylor Polynomials”. In: *AIAA SCITECH 2022 Forum*. San Diego, California: American Institute of Aeronautics and Astronautics, Jan. 2022, pp. 1–16. ISBN: 978-1-62410-631-6. DOI: [10.2514/6.2022-0859](https://doi.org/10.2514/6.2022-0859). URL: <https://arc.aiaa.org/doi/10.2514/6.2022-0859>.
- [11] Kaushik Prabhu, Manoranjan Majji, and Kyle T. Alfriend. “Least Sum of Absolute Residuals Orbit Determination”. In: *Journal of Guidance, Control, and Dynamics* 45.3 (Mar. 2022), pp. 468–480. ISSN: 1533-3884. DOI: [10.2514/1.G006088](https://doi.org/10.2514/1.G006088). URL: <https://arc.aiaa.org/doi/10.2514/1.G006088>.
- [12] Matteo Losacco, Alberto Fossà, and Roberto Armellin. “A low-order automatic domain splitting approach for nonlinear uncertainty mapping”. Unpublished results.
- [13] John L. Junkins and Puneet Singla. “How Nonlinear Is It? A Tutorial on Nonlinearity of Orbit and Attitude Dynamics”. In: *The Journal of the Astronautical Sciences* 52.1-2 (Mar. 2004), pp. 7–60. ISSN: 0021-9142. DOI: [10.1007/BF03546420](https://doi.org/10.1007/BF03546420). URL: <https://link.springer.com/article/10.1007/BF03546420> <https://link.springer.com/10.1007/BF03546420>.
- [14] P. S. Laplace. *Memoires de l’Académie Royale des Sciences de Paris*. 1780.
- [15] C. F. Gauss. *Theoria Motus Corporum Coelestium in Sectionibus Conicis Solem Ambientium*. Cambridge University Press, 1809.

- [16] Laura Pirovano et al. “Probabilistic data association: the orbit set”. In: *Celestial Mechanics and Dynamical Astronomy* 132.15 (Feb. 2020), p. 27. ISSN: 0923-2958. DOI: [10.1007/s10569-020-9951-z](https://doi.org/10.1007/s10569-020-9951-z). URL: <http://link.springer.com/10.1007/s10569-020-9951-z>.
- [17] Dario Izzo. “Revisiting Lambert’s problem”. In: *Celestial Mechanics and Dynamical Astronomy* 121.1 (Jan. 2015), pp. 1–15. ISSN: 0923-2958. DOI: [10.1007/s10569-014-9587-y](https://doi.org/10.1007/s10569-014-9587-y). arXiv: [1403.2705](https://arxiv.org/abs/1403.2705). URL: <http://link.springer.com/10.1007/s10569-014-9587-y>.
- [18] Roberto Armellin, David Gondelach, and Juan Felix San Juan. “Multiple Revolution Perturbed Lambert Problem Solvers”. In: *Journal of Guidance, Control, and Dynamics* 41.9 (Sept. 2018), pp. 2019–2032. ISSN: 0731-5090. DOI: [10.2514/1.G003531](https://doi.org/10.2514/1.G003531). URL: <https://arc.aiaa.org/doi/10.2514/1.G003531>.
- [19] Byron D. Tapley, Bob E. Schutz, and George H. Born. *Statistical Orbit Determination*. Elsevier, 2004, p. 547. ISBN: 9780126836301. DOI: [10.1016/B978-0-12-683630-1.X5019-X](https://doi.org/10.1016/B978-0-12-683630-1.X5019-X). URL: <https://linkinghub.elsevier.com/retrieve/pii/B9780126836301X5019X>.
- [20] David A. Vallado et al. “Revisiting Spacetrack Report #3”. In: *AIAA/AAS Astrodynamics Specialist Conference and Exhibit*. Keystone, Colorado: American Institute of Aeronautics and Astronautics, Aug. 2006, pp. 1–88. ISBN: 978-1-62410-048-2. DOI: [10.2514/6.2006-6753](https://doi.org/10.2514/6.2006-6753). URL: <https://arc.aiaa.org/doi/10.2514/6.2006-6753>.
- [21] Richard H. Battin. *An Introduction to the Mathematics and Methods of Astrodynamics, Revised Edition*. Reston, VA: American Institute of Aeronautics and Astronautics, Jan. 1999, p. 799. ISBN: 978-1-56347-342-5. DOI: [10.2514/4.861543](https://doi.org/10.2514/4.861543). URL: <https://arc.aiaa.org/doi/book/10.2514/4.861543>.
- [22] Joshua T. Horwood, Nathan D. Aragon, and Aubrey B. Poore. “Gaussian Sum Filters for Space Surveillance: Theory and Simulations”. In: *Journal of Guidance, Control, and Dynamics* 34.6 (Nov. 2011), pp. 1839–1851. ISSN: 0731-5090. DOI: [10.2514/1.53793](https://doi.org/10.2514/1.53793). URL: <https://arc.aiaa.org/doi/10.2514/1.53793>.
- [23] Alberto Fossà et al. “Multifidelity Orbit Uncertainty Propagation using Taylor Polynomials”. preprint on arXiv. 2022. DOI: [10.48550/ARXIV.2203.15559](https://doi.org/10.48550/ARXIV.2203.15559). URL: <https://arxiv.org/abs/2203.15559>.
- [24] Alberto Fossà et al. “Combining Taylor polynomials and multifidelity dynamics for the efficient propagation of uncertainties in orbital mechanics”. In: *KePASSA-22, 5th International Workshop on Key Topics in Orbit Propagation applied to Space Situational Awareness*. Ed. by Rosario López, Juan

- Félix San-Juan, and Martin Lara. Logroño, Spain: Universidad de La Rioja, 2022, pp. 114–116. ISBN: 978-84-09-42904-2. URL: <https://dialnet.unirioja.es/servlet/libro?codigo=866643>.
- [25] Jorge J. Moré, Burton S. Garbow, and Kenneth E. Hillstrom. *User Guide for MINPACK-1*. Tech. rep. Argonne, IL: Argonne National Laboratory, 1980, p. 261. URL: <https://cds.cern.ch/record/126569/files/CM-P00068642.pdf>.
- [26] Barr Rosenberg and Daryl Carlson. “A simple approximation of the sampling distribution of least absolute residuals regression estimates”. In: *Communications in Statistics - Simulation and Computation* 6.4 (1977), pp. 421–437. DOI: [10.1080/03610917708812055](https://doi.org/10.1080/03610917708812055). URL: <https://doi.org/10.1080/03610917708812055>.
- [27] Michel Boër et al. “TAROT: a network for space surveillance and tracking operations”. In: *7th European Conference on Space Debris*. Ed. by T. Flohrer and F. Schmitz. Darmstadt, Germany, Mar. 2017, p. 11. URL: <https://conference.sdo.esoc.esa.int/proceedings/sdc7/paper/382/SDC7-paper382.pdf>.
- [28] S A Holmes and W E Featherstone. “A unified approach to the Clenshaw summation and the recursive computation of very high degree and order normalised associated Legendre functions”. In: *Journal of Geodesy* 76.5 (May 2002), pp. 279–299. ISSN: 0949-7714. DOI: [10.1007/s00190-002-0216-2](https://doi.org/10.1007/s00190-002-0216-2). URL: <http://link.springer.com/10.1007/s00190-002-0216-2>.
- [29] Ryan S. Park et al. “The JPL Planetary and Lunar Ephemerides DE440 and DE441”. In: *The Astronomical Journal* 161.3 (Mar. 2021), p. 105. ISSN: 0004-6256. DOI: [10.3847/1538-3881/abd414](https://doi.org/10.3847/1538-3881/abd414). URL: <https://iopscience.iop.org/article/10.3847/1538-3881/abd414/meta%20https://iopscience.iop.org/article/10.3847/1538-3881/abd414>.
- [30] Isadore Harris and Wolfgang Priester. “Time-Dependent Structure of the Upper Atmosphere”. In: *Journal of the Atmospheric Sciences* 19.4 (July 1962), pp. 286–301. ISSN: 0022-4928. DOI: [10.1175/1520-0469\(1962\)019<0286:TDS0TU>2.0.CO;2](https://doi.org/10.1175/1520-0469(1962)019<0286:TDS0TU>2.0.CO;2). URL: [http://journals.ametsoc.org/doi/10.1175/1520-0469\(1962\)019%5C%3C0286:TDS0TU%5C%3E2.0.CO;2](http://journals.ametsoc.org/doi/10.1175/1520-0469(1962)019%5C%3C0286:TDS0TU%5C%3E2.0.CO;2).
- [31] Ch Hubaux et al. “Symplectic integration of space debris motion considering several Earth’s shadowing models”. In: *Advances in Space Research* 49.10 (May 2012), pp. 1472–1486. ISSN: 02731177. DOI: [10.1016/j.asr.2012.02.009](https://doi.org/10.1016/j.asr.2012.02.009). URL: <https://linkinghub.elsevier.com/retrieve/pii/S0273117712001081>.